



Energy-time ptychography for one-dimensional phase retrieval

ANKITA NEGI,^{1,2,*} © LEON MERTEN LOHSE,^{1,2} © SVEN VELTEN,¹ © ILYA SERGEEV,¹ OLAF LEUPOLD,¹ SAKSHATH SADASHIVAIAH,^{3,4} © DIMITRIOS BESSAS,⁵ © ALEKSANDR CHUMAKHOV,⁵ CHRISTINA BRANDT,⁶ © LARS BOCKLAGE,^{1,2} © GUIDO MEIER,^{7,2} © AND RALF RÖHLSBERGER^{1,2,3,4,8} ©

Received 29 May 2025; revised 10 August 2025; accepted 18 August 2025; published 16 September 2025

Phase retrieval is at the heart of adaptive optics and modern high-resolution imaging. Without phase information, optical systems are limited to intensity-only measurements, hindering full reconstruction of object structures and wavefront dynamics essential for advanced applications. Here, we address a one-dimensional phase problem linking energy and time, which arises in X-ray scattering from ultrasharp nuclear resonances. We leverage the Mössbauer effect, where nuclei scatter radiation without energy loss to the lattice and are sensitive to their magneto-chemical environments. Rather than using traditional spectroscopy with radioactive gamma-ray sources, we measure nuclear forward scattering of synchrotron X-ray pulses in the time domain, providing superior sensitivity and faster data acquisition. Extracting spectral information from a single measurement is challenging due to the missing phase information, typically requiring extensive modeling. Instead, we use multiple energetically overlapping measurements to retrieve both the transmission spectrum and the phase of the scattering response, similar to ptychographic phase retrieval in imaging. Our robust approach can overcome the bandwidth limitations of gamma-ray sources, opening new research directions, to the best of our knowledge, with modern X-ray sources and Mössbauer isotopes.

Published by Optica Publishing Group under the terms of the Creative Commons Attribution 4.0 License. Further distribution of this work must maintain attribution to the author(s) and the published article's title, journal citation, and DOI.

https://doi.org/10.1364/OPTICA.568949

1. INTRODUCTION

A fundamental challenge in photon science is the loss of phase information of the electromagnetic wavefield during measurement. This phase problem plagues the study of light–matter interactions across various energy scales and disciplines, e.g., in radar imaging [1,2], astronomy [3,4], microscopy [5–8], and crystallography [9]. It also appears in imaging methods using electrons [10] and neutrons [11]. It arises because no detector can directly sample the electromagnetic field oscillations of optical and X-ray light. For instance, even the most advanced X-ray detectors, such as microchannel plates, can only capture the intensity of the wavefield averaged over time windows greater than 10 ps [12,13]. Meanwhile, reliable algorithms have been developed to retrieve the phase in two dimensions (e.g., diffraction imaging [14–16]) and higher dimensions (e.g., crystallography [17]). The one-dimensional phase problem is highly ill-posed and inherently

more challenging to solve due to multiple non-trivial ambiguities [18]. The mathematical proof is derived from D'Alembert's fundamental theorem of algebra, which states that, unlike single-variable polynomials, multidimensional polynomials are generally not factorable [19]. Unlike higher-dimensional problems, it is typically not possible to uniquely solve a one-dimensional phase problem using only one measurement, even when prior information such as non-negativity is assumed [20].

One-dimensional phase problems arise, for example, in ultrafast laser pulse diagnostics [21,22]. The laser pulse is only a few femtoseconds long, and its temporal response cannot be measured directly. Instead, the pulse is gated with itself in time with the help of a non-linear optical medium, and its frequency spectrum is measured for different time delays. The temporal shape and length of the pulse are then retrieved from this two-dimensional dataset, which is called the frequency-resolved optically gated

¹Department of Photon Science, Deutsches Elektronen-Synchrotron DESY, Notkestr. 85, 22607, Hamburg, Germany

²The Hamburg Centre for Ultrafast Imaging, Luruper Chaussee 149, 22761 Hamburg, Germany

³Helmholtz Institute Jena, Fraunhoferstr. 8, 07743, Jena, Germany

⁴GSI Helmholtz Centre for Heavy Ion Research, Planckstr. 1, 64291, Darmstadt, Germany

⁵European Synchrotron Radiation Facility, F-38043 Grenoble, France

⁶Institute for Mathematics and Informatics, University of Greifswald, Walther-Rathenau-str. 47, 17489 Greifswald, Germany

Max Planck Institute for the Structure and Dynamics of Matter, Luruper Chaussee 149, 22761 Hamburg, Germany

⁸Institute of Optics and Quantum Electronics, University of Jena, Max-Wien-Platz 1, 07743, Jena, Germany *ankita.negi@desy.de

(FROG) trace [23], using a phase retrieval algorithm based on the short-time Fourier transform [24]. Another example is the Griffin–Lim algorithm, which is used to separate speech signals from background noise in two-dimensional audio spectrograms [25].

An analogous problem arises in Mössbauer physics, when the nuclear forward scattering (NFS) signal of an object is measured. The recoilless scattering of X-ray photons by nuclei, known as the Mössbauer effect [26], offers unique insights [27–30] into the magnetic and electronic structure of materials. The sharp natural linewidth of the nuclear transitions allows for extraordinary energy resolutions $(10^{-13}-10^{-8} \text{ eV})$ compared to electron spectroscopy methods $(10^{-2}-10^{-1} \text{ eV})$ [31,32]. For example, the 14.4 keV transition in the iron isotope ⁵⁷Fe has an extremely narrow natural linewidth $\Gamma = 4.7$ neV, corresponding to a quality factor of $\sim 10^{12}$. Conventional lab-based methods for measuring the energy spectrum of these sharp transitions are unsuitable for materials with unavailable or short-lived radioactive sources [30,33] and for experiments requiring a small focused beam [34,35]. For the energy-resolved study of 57 Fe-containing materials, synchrotron Mössbauer source (SMS) setups [36,37] that use pure nuclear Bragg reflections from a ⁵⁷FeBO₃ crystal have been developed. This technique enables ⁵⁷Fe Mössbauer spectroscopy at synchrotrons but introduces other challenges. The Doppler motion of the crystal to tune the energy often causes fluctuations in the reflected beam due to crystal imperfections. Moreover, maintaining the temperature stability of the setup is critical for achieving high energy resolution $(3-6\Gamma)$. In addition, high resolution reduces photon flux, resulting in a trade-off between resolution and intensity [38].

Instead, the sub-100 ps X-ray pulses from advanced synchrotron sources can be used directly to study nuclear transitions in the time domain. These pulses, with energy bandwidths monochromatized to approximately 1 meV ($\approx 10^4$ times the hyperfine splitting of the resonances), contain fewer than 0.01 resonant photons per pulse. As the synchrotron pulse traverses an object, the entire nuclear ensemble coherently scatters a single resonant X-ray photon, forming a nuclear exciton–polariton [39–41]. Following this excitation, the exciton undergoes collective evolution and spontaneous decay, resulting in the emission of photons at delayed times. The linear response of the object to the weak driving field is described in the energy domain as $\hat{E}_s(\omega) = \hat{O}(\omega)\hat{E}_{in}(\omega)$, where \hat{E}_{in} and \hat{E}_{s} represent the energy spectra of the input and scattered X-ray fields, respectively, and $\hat{O}(\omega)$ is the transmission function of the object. For X-rays of wavelength $2\pi/k$ passing through an object of thickness z, the transmission function is given as follows:

$$\hat{O}(\omega) = e^{-i\chi_0(\omega)kz}.$$
 (1)

It is inherently complex due to the complex susceptibility χ_0 of the nuclear transition [39,42]. We can assume that all spectral components $\hat{E}_{\rm in}$ of the input synchrotron pulse have an equal magnitude E_0 within the narrow energy bandwidth of the monochromatization. The scattered field E_s is then related to the object's transmission function \hat{O} as

$$E_s(t) \propto \mathcal{F}\{\hat{E}_s(\omega)\} = E_0 \mathcal{F}\{\hat{O}(\omega)\},\tag{2}$$

where \mathcal{F} denotes the Fourier transform from the energy to the time domain. In the timing mode of operation, the filling pattern of

the electron storage ring is chosen such that synchrotron pulses are temporally spaced at intervals longer than the lifetime of the nuclear transitions. Avalanche photodiodes detect delayed photons as a function of time after excitation, and the measured signal is proportional to the intensity of the scattered field $|E_s(t)|^2$. The hyperfine structure of the object manifests itself in the beating patterns of this temporal response.

Despite advances in data analysis software and modeling [43,44], interpreting the time-domain response of NFS to extract the different hyperfine parameters remains challenging. On the other hand, if phase information of the photons is available, the inverse Fourier transform can yield the complex energy spectrum of an object from NFS measurements without relying on a fit model or SMS setups. Furthermore, the energy resolution is not limited by the bandwidth of the crystal reflection in the SMS setup. However, the phase shift experienced by the scattered X-ray wavefield is lost in these measurement techniques, presenting a one-dimensional phase problem.

Various methods have been developed to tackle this phase problem in nuclear resonant scattering. For example, interferometry has been attempted to measure the phase shifts of a nuclear forward scattering object using a triple Laue interferometer [45,46]. However, the short wavelengths and near-unity refractive indices of most materials in the X-ray regime make designing and stabilizing such interferometers highly challenging. Contemporary approaches substitute the interferometer with a probe sample mounted on a Doppler drive, where the Doppler drive serves as the phase shifter, and the object and probe samples act as interferometer arms. Techniques such as heterodyne phase reconstruction (HPR) [47] and frequency-frequency correlation [48] are based on this setup, but are only applicable when the nuclear resonances of the probe and the object samples are so detuned in energy that their radiative coupling [41,49,50] can be neglected. Additionally, these methods require a probing beam with a narrow single-energy line, which is scanned in small detuning steps across the object to improve energy resolution. The probe beam can be generated using a nuclear scattering sample that acts as a two-level quantum system. However, to achieve this, it is difficult to eliminate the residual hyperfine interaction in quasi-single-line absorbers such as ⁵⁷Fe-based stainless steel [51].

In this paper, we propose performing ptychography to retrieve the one-dimensional phase of an object. Ptychography is a scanning technique that uses multiple overlapping measurements to constrain the phase problem, and is commonly implemented in the field of X-ray diffraction imaging [52]. It is a mathematical cousin of the short-time Fourier transform, but has less stringent scanning requirements. For nuclear ptychography, the probe has a broad energy spectrum and can illuminate a wide energy range on the object, allowing the scanning of the object spectrum with fewer measurements. The overlap between the measurements is set by the energy detuning of the probe with respect to the object.

Early conceptual work on a phase-sensitive ptychographic method for nuclear resonant systems by Haber [53] recognized its potential in the emerging field of hard X-ray quantum optics with nuclear exciton polaritons, which exhibit long coherence times and unique quantum behaviors [54–57] and inspire research in fundamental physics [58,59] and quantum information [60,61]. Accessing the spectral phase provides insight into the coherence properties of the excitonic state, which is key to its manipulation and control [62–64]. For example, the phase can help distinguish

between incoherent line-broadening due to thickness effects and coherent features due to hyperfine distributions in the transmission spectrum.

In two-dimensional phase problems, blind ptychography approaches [65,66] are widely used to simultaneously retrieve both the object and probe. A recent publication by Yuan et al. [67] extends this idea to nuclear resonant systems using blind and partially blind algorithms with a thin (1 µm) K₂Mg⁵⁷Fe(CN)₆ analyzer as the probe. However, these blind methods are reported to not outperform the fixed probe method in terms of reconstruction quality. In contrast, our experiment uses a ~20 µm thick, ⁵⁷Fe-enriched stainless-steel foil as the probe, with dynamical beats [68] in its time response. This thickness was deliberately chosen to maximize the nuclear resonant signal of the probe. The object transmission spectrum contained six well-separated ⁵⁷Fe resonances, which was too sparse to support reliable simultaneous probe retrieval. Instead, we fixed a physics-informed model of the probe, including hyperfine splittings, into our reconstruction algorithm. This fixed-probe approach enables a more interpretable and stable inversion by allowing us to isolate and examine core aspects of signal formation and reconstruction limits and reflects our focus on experimental realism and robustness.

Similarly to how ptychographic imaging has advanced spatial resolution in diffraction-limited systems [69–71], we propose that the development of a ptychographic spectroscopy method could unlock new resolution regimes for Mössbauer science.

2. PTYCHOGRAPHY USING RESONANT SCATTERING BY A TWO-SAMPLE SYSTEM

The goal of ptychography is to retrieve the complex object transmission function $\hat{O}(\omega)$. To achieve this, a probe sample is placed in front of the object sample in the X-ray beam path (Fig. 1). In imaging setups, the probing beam is shaped by a lens or aperture that spatially restricts the illumination to a localized spot on the object. In our setup, the probe transmission function $\hat{P}(\omega)$ must have a spectral width comparable to that of the hyperfine splittings of nuclear levels in the X-ray regime. A suitable choice is a quasisingle-line absorber, such as stainless steel, whose thickness can be adjusted to achieve the desired spectral width.

Next, a mechanism is required to energetically detune the probe with respect to the object, so that a different energy range in the object spectrum is illuminated for each ptychographic measurement. This can be achieved via the Doppler effect if either the object sample or the probe sample is moved with respect to the other along the direction of beam propagation. This motion induces an additional time-dependent phase shift in the radiation scattered by the probe sample:

$$\varphi(D, t) = \frac{2\pi}{\lambda} |\vec{v}|t = Dt, \tag{3}$$

where λ is the wavelength of the X-rays, and $D = 2\pi |\vec{v}|/\lambda$ is the Doppler shift (in angular frequency) induced by the relative motion with velocity \vec{v} . The combined transmission function of the probe-object sample system is given as

$$\hat{Z}(D,\omega) = \hat{P}(\omega + D) \cdot \hat{O}(\omega). \tag{4}$$

Assuming that all detected photons are coherently scattered, the intensity at the detector at any time is equal to the squared magnitude of the scattered wavefield and can be modeled as

$$I(D, t) \propto \left| \mathcal{F}\{\hat{P}(\omega + D) \cdot \hat{O}(\omega)\} \right|^2.$$
 (5)

This is the one-dimensional continuous ptychographic forward model. It is non-linear due to the presence of the modulus squared $|\cdot|^2$ operator. Inverting Eq. (5) to obtain the complex object function $\hat{O}(\omega)$ is impossible using only one measurement. Even by imposing prior constraints on $\hat{O}(\omega)$, such as compact support or sparsity, the one-dimensional phase problem can have an infinite number of solutions and is unstable [72,73]. However, it is possible to use data diversity to impose the overlap constraint [65] in Eq. (5). Multiple related measurements are taken by changing the detuning D so that the probed parts of the object overlap in energy, as shown in Fig. 1. This scheme of time- and energyresolved measurement of the scattering process encodes the phase of the one-dimensional object in a two-dimensional ptychographic dataset called a "ptychogram" [74] and may be recovered using a decoding algorithm. It is analogous to a traditional spectrogram that encodes the variation in a signal's frequency content with time.

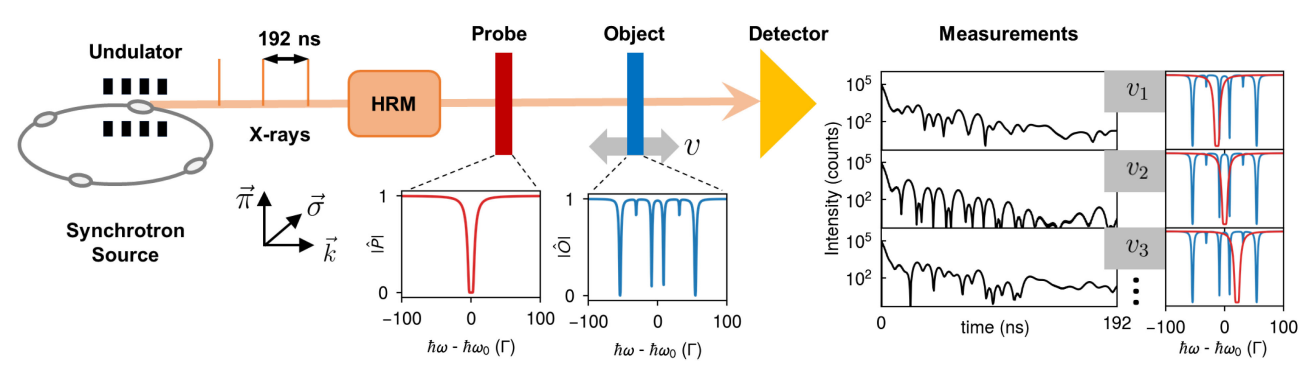


Fig. 1. Ptychography scheme for nuclear forward scattering: pulsed X-ray radiation is generated from the synchrotron source with wave vector \vec{k} and linear polarization along $\vec{\sigma}$. It is monochromatized by a high-resolution monochromator (HRM) to a bandwidth of 1 meV around the nuclear resonance ($\hbar\omega_0=14.4~{\rm keV}$). A probe sample is mounted in front of an object sample and either of the two is moved with respect to the other with a velocity $\vec{v} \parallel \vec{k}$ using a Doppler drive. The X-ray pulses are scattered by the nuclei in the two samples. The magnitude of the transmission spectrum of the probe \hat{P} and object \hat{O} is shown in the insets. The detector measures the combined response of the samples as counts of photons scattered over time. Changing the velocity of the Doppler drive changes the relative detuning of the samples in the energy domain and leads to a different temporal response at the detector. This allows multiple intensity measurements (shown for different velocities v_1, v_2, v_3, \ldots) to be collected.

In ptychographic imaging setups, smaller spatial features in a sample result in larger scattering angles in detected diffraction patterns. The largest scattering angle that the detector can capture sets the minimum achievable spatial resolution for the reconstruction. In the nuclear ptychography setup, an analogous constraint arises due to the maximum acquisition time $T_{\rm max}$ at the detector, which is determined by the finite time interval between synchrotron pulses. This imposes a limit on the maximum achievable energy resolution of the reconstructed object spectrum (in units of Γ):

$$\hbar \Delta \omega' = \frac{2\pi}{T_{\text{max}}} \cdot \frac{\hbar}{\Gamma} = 2\pi \cdot \frac{\tau}{T_{\text{max}}},\tag{6}$$

where $\tau = \hbar / \Gamma$ is the lifetime of the excited nuclear state. Because nuclear transitions are extremely sharp in energy, their time response can extend beyond $T_{\rm max}$, fundamentally limiting the energy resolution of this technique. This contrasts with imaging experiments in which the resolution is typically constrained by factors such as the radiation dose on the sample [75], decoherence effects [76], and Poisson noise, rather than detector size.

3. DECODING SCHEME

The ptychogram can be inverted using numerical algorithms, for which we discretely approximate the continuous phase problem in Eq. (5). The discrete object and probe functions are expressed as one-dimensional arrays $\hat{\mathbf{O}} \in \mathbb{C}^N$, $\hat{\mathbf{P}} \in \mathbb{C}^N$ on an energy grid of length N and resolution $\Delta \omega$. We take $j=1, 2 \cdots M$ measurements corresponding to different probe detunings D_j and detuned probe functions $\hat{\mathbf{P}}_{j,i} = \hat{\mathbf{P}}(\omega_i, D_j)$. The intensity in the time domain is measured and binned into N time points with a fixed interval Δt and modeled as $\mathbf{I}_j \in \mathbb{R}^N$. The phase problem can now be formulated as an optimization problem to solve for an object $\hat{\mathbf{O}}$ that minimizes a cost function $\rho: X \to [0, \infty)$ given by

$$\rho(\hat{\mathbf{O}}) = \sum_{j=1}^{M} \left\| \sqrt{\mathbf{I}_{j}} - \sqrt{\mathbf{b}_{j}} \right\|^{2}$$

$$= \sum_{j=1}^{M} \left\| \left| \mathbf{F} \{ \hat{\mathbf{P}}_{j} \circ \hat{\mathbf{O}} \} \right| - \sqrt{\mathbf{b}_{j}} \right\|^{2}, \tag{7}$$

where F represents the discrete Fourier transform, o denotes pointwise multiplication, and $\|\cdot\|$ denotes the ℓ^2 norm. The cost function represents the distance between the measured intensities \boldsymbol{b}_i and the modeled intensities \boldsymbol{I}_i of the ptychogram and is based on the Poisson likelihood model for noise in the ptychogram ([77], Section 4 of Supplement 1). In Eq. (7), we optimize an object of grid size $N \sim 10^3$, where global optimization methods struggle due to the curse of dimensionality [78,79]. Therefore, a local search with gradient descent is performed to minimize ρ by using its local gradient with respect to the object [80]. Owing to the non-convexity of the cost function ρ , the gradient descent algorithm may converge to local minima, and the uniqueness of the solution is not guaranteed. To mitigate slow convergence, we incorporate a stochastic gradient descent (SGD) algorithm where the ptychogram dataset is shuffled and divided into random "mini-batches" whose gradients are used to update the object [81]. In our case, we observe that SGD converges noisier than the classic gradient descent, but it achieves an optimum with an order of magnitude fewer iterations. We implemented the reconstruction

algorithm for nuclear ptychography in a software package, which we call NuPty [82]. All NuPty algorithms were implemented using PyTorch [83]. This enables a flexible and faster analysis of the phase problem because PyTorch uses its automatic differentiation capabilities to efficiently compute gradients and supports GPU-accelerated computations. The NuPty reconstruction scheme takes into account two key nuances of the ptychography experiment:

A. Multimodal Ptychography Model

Thickness variations in the transmitting probe sample may introduce several incoherent scattering paths into the setup. To account for this, the intensity at the detector is modeled as an incoherent superposition of the intensities of the scattered fields corresponding to different probe modes m illuminating the object [84,85], i.e., in Eq. (7):

$$I_{j} = \sum_{m} w_{m} \left| \mathbf{F} \left\{ \hat{\boldsymbol{P}}_{j}^{(m)} \circ \hat{\boldsymbol{O}} \right\} \right|^{2}, \tag{8}$$

where w_m is a scalar denoting the relative weight of each probe mode $\hat{\pmb{P}}_j^{(m)}$.

B. Time Window

Nuclear resonant scattering occurs with a delay (ns timescale) compared with prompt electronic scattering (ps timescale). The time-resolving detector is synchronized to the synchrotron bunch clock and resets to zero when a new X-ray pulse hits the sample. To prevent the prompt signal from saturating the detection system, a veto interval is set around the bunch clock, establishing a data acquisition time window from T_{\min} to T_{\max} for the nuclear scattered signal. To ensure that the reconstruction result is scale-independent with respect to the number of photons $N_{\rm ph}$ detected in the time window, the algorithm uses a normalized form of the cost function:

$$\tilde{\rho}(\hat{\boldsymbol{O}}) = \frac{1}{B \cdot f_{\text{ph}} \cdot L} \sum_{i=1}^{B} \left\| \sqrt{\boldsymbol{W} \circ \boldsymbol{I}_{i}} - \sqrt{\frac{M \cdot \|\mathbf{F}\|^{2}}{N_{\text{ph}}/f_{\text{ph}}} \cdot \boldsymbol{b}_{i}}} \right\|^{2}. \quad (9)$$

Here, B is the batch-size, i.e., the number of measurements used at a time to update the gradient, M is the total number of measurements, and $L = (T_{\rm max} - T_{\rm min})/\Delta t$. To speed up the calculations of the ptychogram and the cost function, we use the fast Fourier transform (FFT) with the operator norm $\| {\bf F} \| = N$. The symbol $f_{\rm ph}$ denotes the probability of photon scattering within the time window:

$$\mathbf{W}(t_i) = \begin{cases} 1 & T_{\min} \le t_i \le T_{\max}, \\ 0 & \text{otherwise.} \end{cases}$$
 (10)

This probability can be calculated through simulations of the experimental setup, and an order-of-magnitude estimate is sufficient for practical purposes.

4. SIMULATION

To benchmark the phase retrieval algorithm, a simulation of the experiment was performed using the NEXUS software package [44] and is shown in Fig. 2(a). A stainless-steel foil with an enrichment 95% ⁵⁷Fe and a thickness 20 µm was taken as the probe sample. As shown in Fig. S2 of Supplement 1, this thickness

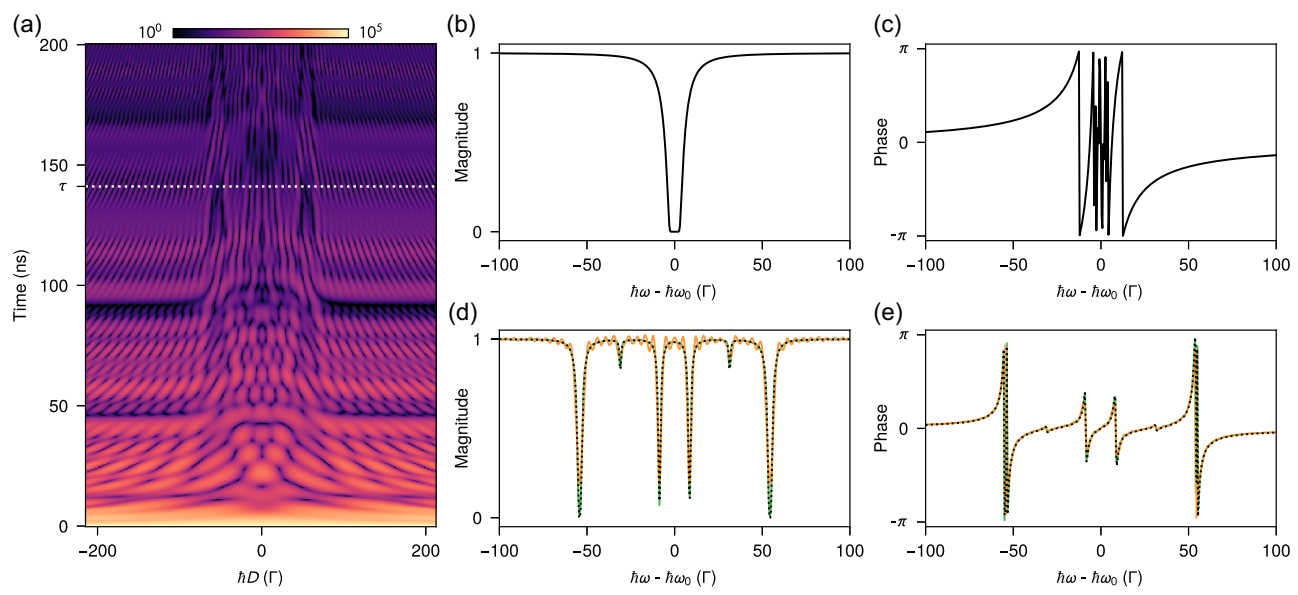


Fig. 2. Phase retrieval from simulation: (a) ptychogram simulated as described in Section 4. The dotted white line marks $\tau = 141$ ns, which is the lifetime of the 14.4 keV energy level of the ⁵⁷Fe nucleus. The magnitude (b) and phase (c) of the probe spectrum are shown. (d) The magnitude of the transmission spectrum of the reconstructed object is plotted for $T_{\text{max}} = 200$ ns (orange) and $T_{\text{max}} = 1000$ ns (green). The reconstructed spectrum in green overlaps perfectly with the true object spectrum (dotted black line). For lower T_{max} , artificial peaks appear in the reconstructed spectrum. (e) Reconstructed phase spectrum for the two values of T_{max} , showing distinct phase shifts at each resonance line. In the plots, $\hbar\omega_0$ refers to the energy of the photons at resonance, i.e., 14.4 keV.

maximizes the nuclear resonant signal of the foil by balancing the trade-off between increased number of nuclear scatterers and electronic absorption. A 95% enriched ⁵⁷Fe metal foil of thickness 2.5 μ m was taken as the object sample. Figures 2(b)–2(e) represent the simulated energy spectra of the object and the probe samples, respectively. The magnetic structure of the simulated samples is based on the foils used in the real experiment, details of which can be found in Sections 1 and 2 of Supplement 1. The probe absorption function has an almost Lorentzian line profile with a full-width at half-maximum (FWHM) of \sim 10 Γ , providing broad spectral coverage. This ensures sufficient overlap between adjacent measurements, even for coarsely sampled detunings D.

The object transmission function is Zeeman split into six lines. The object sample is also modeled after the experimental values (see Section 5) to contain 94.2(3)% magnetic moments parallel to the $\vec{\sigma}$ direction, which coincides with the linear polarization vector of the incident synchrotron beam, and the remaining 5.8(3)% are isotropically distributed. For both orientations of the magnetic moment, the selection rules of the 14.4 keV ⁵⁷Fe transition prohibit the object sample from being optically active [42]. Therefore, we only aim to reconstruct the spectrum of the $\vec{\sigma} \rightarrow \vec{\sigma}$ scattering channel. All other entries in the scattering matrix are zero.

To simulate the time-domain scattering signal and perform Fourier transforms efficiently, we used the discrete fast Fourier transform (FFT). The number of points $N_{\rm FFT}$ used in the fast Fourier transform (FFT) of the time-domain signal determines its energy resolution as

$$\hbar\Delta\omega = \frac{2\pi}{N_{\rm FFT} \cdot \Delta t} \cdot \frac{\hbar}{\Gamma},\tag{11}$$

where Δt denotes discretization of the temporal grid. To accurately compute the linear convolution of the probe and object signals of length N, $N_{\text{FFT}} > 2N-1$ to prevent circular convolution errors.

A large $N_{\rm FFT}$ ensures that $\Delta \omega$ is sufficiently small to resolve the sharp spectral peaks and avoid aliasing errors.

During the experiment, the energy resolution is fundamentally limited by the maximum acquisition time $T_{\rm max}$, as shown in Eq. (6). However, in the simulation, $\hbar\Delta\omega$ can be improved indefinitely by choosing larger values of $N_{\rm FFT}$. For $\Delta t=0.5$ ns, the probe and object spectra are defined in a $N_{\rm FFT}=4096$ point energy grid from $-886.6~\Gamma$ to $886.2~\Gamma$ in $0.4~\Gamma$ steps, where $\Gamma=4.7~{\rm neV}$. The noiseless ptychogram was simulated by detuning the probe spectrum at M=512 different Doppler-shifted energies $\hbar D \in (-200,200)~\Gamma$ with $0.78~\Gamma$ steps. Due to the broad probe energy spectrum, this creates an overlap of $\sim 90\%$ between consecutive measurements.

To evaluate the performance of the phase retrieval algorithm as Poisson noise levels increase, we simulated ptychograms by varying the total delayed photon counts $N_{\rm ph}$ and perform the reconstruction (see Section 5.A of Supplement 1). We found a roughly linear dependence of the reconstruction accuracy on $N_{\rm ph}$, without any anomalies. Thus, the algorithm is stable with respect to increasing levels of Poisson noise.

To investigate the impact of the time window, the number of photons $N_{\rm ph}$ was fixed at 10^9 for the next set of tests, whereas only the maximum acquisition time at the detector, $T_{\rm max}$, was varied (see Section 5.B Supplement 1). The energy discretization of the FFT grid was kept constant at $\hbar\omega=0.4~\Gamma$, and the time-domain calculations were performed with zero-padding. As shown in Figs. 2(d) and 2(e), the reconstructed spectra for both $T_{\rm max}=200~{\rm ns}$ (orange) and $T_{\rm max}=1000~{\rm ns}$ (green) show six inverted peaks at the same positions as the simulated spectrum (dotted black line). The X-ray scattering probability depends on the angle between the nuclear magnetic field and X-ray polarization. The higher intensity of the outermost peaks indicates that

most of the magnetic moments were aligned parallel to the polarization direction. The outermost peak separation ΔE can be used to calculate the magnetic hyperfine field:

$$B_{\rm hf} = \frac{\Delta E}{\mu_N \cdot \left(3|g_{\rm e}| + |g_{\rm g}|\right)},\tag{12}$$

where $g_g = 0.18121$ and $g_e = -0.10348$ are the nuclear g-factors for the ground and excited states of ⁵⁷Fe, and μ_N is the nuclear magneton ($\approx 5.05 \times 10^{-27}$ J/T). The resulting $B_{\rm hf}$ value for both the green and orange curves is 32.7(2) T. For $T_{\rm max} = 200$ ns, which is close to the experimental condition of the bunch spacing (=192 ns), the short time window causes spectral leakage due to sinc interpolation artifacts in the reconstruction. This occurs because zero-padding in the time domain is equivalent to applying a rectangular time window, whose Fourier transform is a Dirichlet kernel. To suppress these artifacts, the measurement time window should extend beyond four nuclear lifetimes between pulses. Additionally, the shortened time window affects both the relative phase shifts and the peak intensities of the resonance spectrum.

5. RESULTS AND DISCUSSION

We conducted a proof-of-principle experiment at the high-resolution dynamics beamline P01 at the PETRA III synchrotron source, providing X-ray pulses at 192 ns intervals in the timing mode of operation. X-rays were monochromatized to one meV bandwidth at the 14.4 keV $^{57}{\rm Fe}$ nuclear transition. The probe and object foils were characterized using NFS measurements. The probe is given by a stainless-steel foil, enriched to 95% in $^{57}{\rm Fe}$, with a Lamb–Mössbauer factor of 0.78. The thickness of the foil approximately follows a normal distribution, centered at 17.8 μm with an FWHM of 0.7 μm . The object under study is an iron metal foil, enriched to 95% in $^{57}{\rm Fe}$, with a Lamb–Mössbauer factor of 0.80 and a mean thickness of 2.4 μm (FWHM 0.3 μm).

The object foil was mounted on a Doppler drive and moved relative to the probe foil with a sinusoidally changing velocity profile. The drive velocity was tuned to a maximum of 20.7 mm s⁻¹, to ensure Doppler detunings in the range $\hbar D \in (-210,210) \Gamma$. A 0.12 T magnetic field ($\vec{B} \parallel \vec{\sigma}$, beam polarization) was applied to the object. Photons were detected using silicon-based avalanche photodiodes with a time resolution of \sim 0.3 ns and binned into time channels such that $\Delta t = 0.5$ ns. Their arrival times were recorded together with the Doppler velocity at the moment of detection using a multichannel data acquisition system. More details on the samples and setup are available in Sections 1 and 2 of Supplement 1.

Phase information was captured in the ptychogram [Fig. 3(a)], with time and Doppler detuning as its axes. The measured dataset closely resembles the simulated ptychogram [Fig. 2(a)], except for the experimental data acquisition window from $T_{\rm min}=17$ ns to $T_{\rm max}=178$ ns. This is due to the vetoing of the electronic scattering signal as described in Section 3. The results of the ptychographic reconstruction using the experimental measurements are also shown in Fig. 3. According to our simulations, the majority of the incident photons undergo prompt electronic scattering within the first few picoseconds. Only a small fraction, $f_{\rm ph}\approx 0.019$, is scattered within the delayed time window, resulting in the detection of approximately 2×10^8 total delayed photons. While reconstructing the object, the algorithm can reasonably extrapolate the missing intensities between 0 and 17 ns by

taking advantage of the oversampled measurements. This is also performed in conventional two-dimensional ptychographic imaging in the presence of a beam stop [86,87]. However, there is no information in the ptychogram for times beyond $T_{\rm max}$, where the extrapolation obviously does not work. For a maximum acquisition time $T_{\rm max}=178$ ns at the detector, the energies of the nuclear transitions are convolved with a sinc function with a main lobe width of $2\hbar\Delta\omega'\approx 9.3~\Gamma$, which is roughly 23 times larger than $\hbar\Delta\omega$. To evaluate the quality of the reconstruction despite the finite $T_{\rm max}$, we define a filtering window ${\pmb H}$, which is a discretized Heaviside step function:

$$\boldsymbol{H}(t_i) = \begin{cases} 1 & t_i \le T_{\text{max}}, \\ 0 & \text{otherwise.} \end{cases}$$
 (13)

Applying this filter to the simulated complex transmission spectrum of the object \hat{O}^* (from Section 4) yields

$$\hat{\boldsymbol{O}}_{H}^{*} = \mathbf{F}^{-1} \{ \boldsymbol{H} \circ \mathbf{F} \{ \hat{\boldsymbol{O}}^{*} \} \}, \tag{14}$$

where **F** is the FFT. The resulting transmission spectrum, \hat{O}_{H}^{*} , accounts for sinc artifacts similar to those caused by the experimental measurement window. In Figs. 3(b) and 3(c), the reconstructed object is compared with this filtered object.

The reconstruction of the complex transmission spectrum from the full data range $\hbar D \in (-210,210) \Gamma$ (orange) deviates from the true object, while the limited range $\hbar D \in (-70,70) \Gamma$ (green) achieves a closer match. We attribute this behavior to the coupling between the resonance peaks of the probe and the object in this regime (see Section 5.C of Supplement 1). This contrasts to the interference signal used in other techniques [47,48] where the probe and object spectra are so tuned that the scattered field at the detector can be approximated as $Z(D,t) = \mathcal{F}\{\hat{Z}(D,\omega)\} \approx P(D,t) + O(t)$, where P(D,t) and O(t) are their respective temporal responses. The coupling signal has a higher information density and is less susceptible to background noise, velocity drive calibration errors, and incoherent contributions to the data from thickness variations in the samples.

The reconstructed phase enables the calculation of an energydomain spectrum for the object which can then be compared to its measured synchrotron Mössbauer source (SMS) spectrum. The positions of the four most prominent Lorentzian lines in Fig. 3(d) are fitted using a least squares peak finding algorithm and are listed in Table 1. The four peak positions extracted from the magnitude of the reconstructed object in green match the SMS spectrum up to $\pm 0.2 \Gamma$, which is comparable to the resolution of the calculation grid (0.4Γ) . According to Eq. (12), the magnetic hyperfine field extracted from the reconstructed outer peak positions is 32.6(2) T, compared to 32.7(2) T extracted from the outer peak positions of the SMS spectrum. To calculate the preferential orientation of the magnetic domains in the ⁵⁷Fe foil, other peak properties, such as their relative heights and symmetry, are needed. Our reconstructed transmission spectrum reveals the presence of a dominant magnetic moment component parallel to the X-ray polarization direction. In Fig. 3(d), two additional small resonance peaks appear in the SMS spectrum at roughly $\pm 31.5 \,\Gamma$, due to a minor isotropic nuclear spin component of 57 Fe ($\approx 5.8(3)\%$ from nuclear forward scattering measurement). Although these smaller peaks cannot be distinguished clearly from the artificial peaks in the reconstructed spectrum, the presence of their subtle signatures

Research Article Vol. 12, No. 9 / September 2025 / Optica 1535

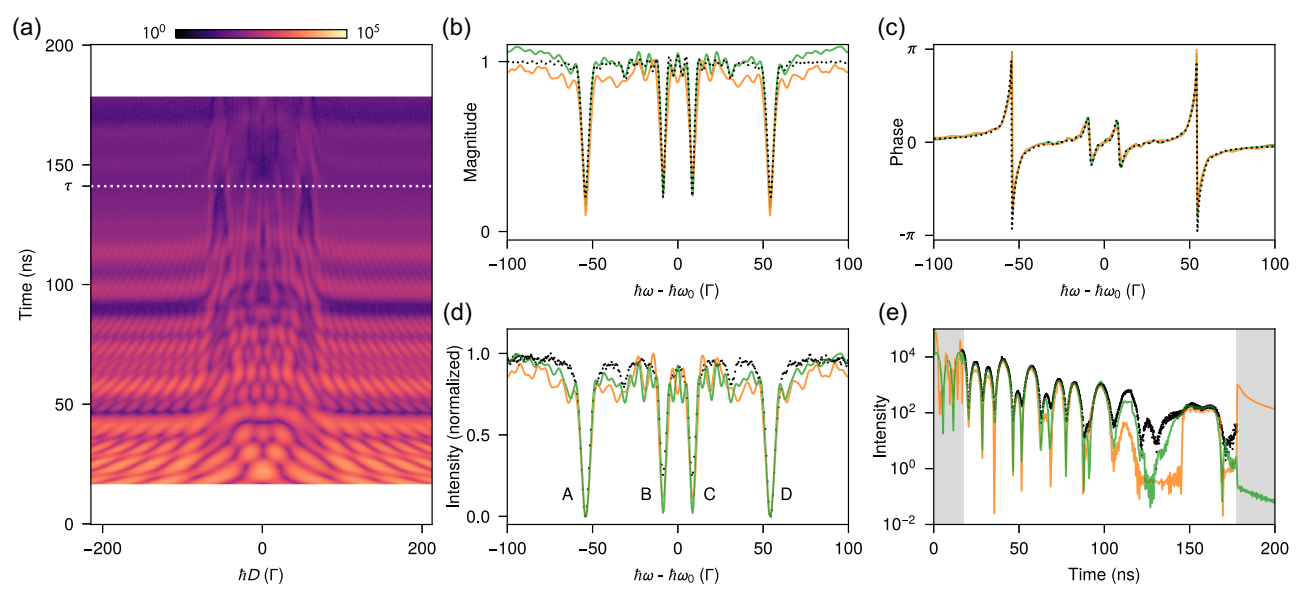


Fig. 3. Phase retrieval from experiment: (a) ptychogram measured in the PETRA III experiment. The dotted white line marks $\tau=141$ ns, which is the lifetime of the 14.4 keV energy level of the ⁵⁷Fe nucleus. (b) Magnitude and (c) phase of the reconstructed object spectra for $|\hbar D_{\text{max}}| = 70 \,\Gamma$ (in green) and $|\hbar D_{\text{max}}| = 210 \,\Gamma$ (in orange) shown alongside the simulated object spectrum $\hat{\textbf{O}}_H^*$ (dotted black line). (d) Intensity spectrum of the reconstructed objects plotted alongside the measured synchrotron Mössbauer spectrum of the ⁵⁷Fe foil used in the experiment. The spectra are normalized from 0 to 1. (e) Time response of the reconstructed objects plotted alongside the measured nuclear forward scattering from the ⁵⁷Fe foil. The gray-shaded region lies outside the data acquisition time window of 17–178 ns.

Table 1. Positions of the Peaks Marked in Fig. 3(d), Determined by a Multi-Lorentzian Peak-Fitting Algorithm

| Peak | A | В | C | D |
|------------------------|-----------------|---------------|-------|--------|
| SMS spectrum | -54.2 Γ | -8.6 Γ | 8.5 Г | 54.4 Γ |
| Reconstruction (green) | -54.1Γ | -8.5Γ | 8.6 Γ | 54.2 Γ |

indicates that nuclear ptychography is already approaching the sensitivity required to detect such fine features, implying a strong potential for further improvements in reconstruction accuracy with longer measurement time windows.

In Fig. 3(e), the time-domain response of the reconstructed object shows that the algorithm accurately reconstructs the measured intensities, except for times between 120 and 140 ns. In this region, "bunch addition" incoherence in the experimental data is strong due to the finite time gap of 192 ns between the incident X-ray pulses (see Section 3.B of Supplement 1). The detector cannot distinguish between photons arriving at t > 192 ns after the incidence of the current pulse and those arriving from the next pulse at t - 192 ns, causing systematic errors in the measured data. This incoherent contribution to the data cannot be taken into account by the ptychography algorithm while solving the phase problem and therefore affects the reconstruction.

The transverse coherence length of the setup is only a few nanometers (see Section 3.A of Supplement 1). The NFS fit on the stainless-steel probe foil predicts a root-mean-square surface thickness variation of approximately 0.7 μ m. Therefore, to reconstruct the object spectrum, the multimodal ptychography model was used, where the complex transmission spectrum of the probe sample was simulated at eleven distinct points sampled from its thickness distribution.

The starting object guess was taken as cells with entry "one." As shown in Fig. 4, the algorithm converges to a solution in less

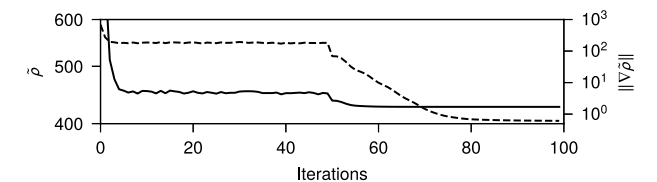


Fig. 4. Convergence of the phase retrieval algorithm: reconstruction cost $\tilde{\rho}$ (solid line) and the norm of its gradient $\|\nabla \tilde{\rho}\|$ (dashed line) as the iterations increase. The algorithm converges to a solution in 100 iterations for the reconstruction from experimental data with $|\hbar D_{\rm max}| = 70~\Gamma$ [shown in green in Figs. 3(b)–3(e)].

than 100 iterations. The first 50 iterations use stochastic gradient descent with a batch size of B=20, leading to rapid improvement within the initial 10 iterations, followed by stagnation at a local minimum. Due to stochastic noise, the gradient no longer decreases significantly. To refine the solution, the remaining 50 iterations employ standard gradient descent (B=M), reducing stochastic noise and enabling further optimization.

6. CONCLUSION AND OUTLOOK

We have demonstrated that ptychography provides a powerful framework to solve a one-dimensional phase problem and mitigate its instabilities by redundantly capturing overlapping information in a two-dimensional dataset. We used the method to reconstruct the complex energy resolved spectrum of a magnetized ⁵⁷Fe foil and calculate its hyperfine parameters. The retrieved values are in good agreement with the results predicted by the established measurement techniques of synchrotron Mössbauer source (SMS) spectroscopy and nuclear forward scattering. Despite the additional complexity introduced by using a thick multimodal probe, our reconstruction algorithm achieves stable convergence in less than 100 iterations. This generalization is especially important

Research Article Vol. 12, No. 9 / September 2025 / Optica 1536

because, in practice, balancing the signal strengths between the probe and the object is necessary to achieve strong interference and clear phase information in the measured ptychogram.

Our analysis shows that the energy resolution of nuclear ptychography is fundamentally related to the length of the temporal detection window. Quantum beats between closely spaced nuclear energy levels, split by less than 1 Γ , interfere on timescales longer than $\tau = \hbar / \Gamma$, the natural lifetime of the Mössbauer nucleus. For detection windows extending beyond $T_{\text{max}} > 2\pi \hbar / \Gamma$, the energy resolution of sub-1 Γ becomes achievable [see Eq. (6)]. Our method can thus surpass the limits set by the linewidth of the lab source of the gamma ray or the SMS crystal. However, to realize this improved resolution, increased pulse spacing between X-ray bunches is required. This, in turn, demands low bunch synchrotron timing modes, which reduce the overall beam current and brightness. The 192 ns X-ray pulse spacing in our experiments, although adequate, was not significantly longer than the lifetime of ⁵⁷Fe and resulted in reconstruction artifacts. Other synchrotrons, such as Spring-8 (Japan) and ESRF (France), operate with pulse intervals more feasible for ⁵⁷Fe nuclear ptychography (see Table S3 of Supplement 1). Moreover, Mössbauer isotopes with shorter lifetimes, such as ¹¹⁹Sn and ¹⁵¹Eu, would particularly benefit from the high resolution offered by nuclear ptychography, since no suitable SMS is available for them. Shorter synchrotron pulse intervals can be chosen to maintain the X-ray brilliance while enabling measurement of delayed responses over multiple lifetimes of these

In conclusion, we have shown that one-dimensional nuclear ptychography provides a robust and versatile tool for exploring complex nuclear resonant phenomena. We can retrieve the spectral phase of the nuclear resonant scattering, which provides direct insight into how an X-ray pulse is reshaped in time as it passes through the nuclear system. This phase information is essential for understanding and engineering coherent phenomena, such as electromagnetically induced transparency-like behavior in multilayered X-ray cavities with Mössbauer nuclei [54,88], where sharp energy-dependent phase shifts from multiple scattering modulate the effective driving field on the nuclei. Beyond solving the phase problem, nuclear ptychography can enable sublinewidth energy resolution and spectroscopic investigation of Mössbauer isotopes at synchrotrons, offering a pathway to resolve elusive features in nuclear spectra, such as the debated existence of magnetic order in hcp-iron [89,90]. Our results pave the way for advanced implementations of this method in grazing-incidence and polarization-resolved geometries, enabling the study of nanostructured and anisotropic systems. The extension of the technique to X-ray free electron lasers, with their exceptional brilliance and unique time structures, offers exciting opportunities to study non-linear effects on the phase of the scattering. Together, these capabilities represent a significant step toward a new era in nuclear quantum optics.

Funding. Helmholtz Association [G:(DE-HGF) 2019_IVF-HIDSS-0002]; Hamburg Centre for Ultrafast Imaging [G:(GEPRIS) 390715994].

Acknowledgment. We thank Mr. J. P. Celse for his technical assistance during the beamtime at ESRF and Dr. Sergey Yaroslavtsev for helpful discussions regarding the analysis of the Synchrotron Mössbauer spectrum of the sample. We also thank Mr. Boris Fiedler for his excellent technical support with electronics. We acknowledge synchrotron beamtime provision by Deutsches Elektronen-Synchrotron (DESY, P01) for proposal I-20210761 and European Synchrotron Radiation Facility (ESRF, ID14) for proposal MI-1420. Ankita Negi, Ralf Röhlsberger, Guido Meier, and Christina Brandt acknowledge DESY (Hamburg,

Germany), a member of the Helmholtz Association HGF, and DASHH, Data Science in Hamburg-Helmholtz Graduate School for the Structure of Matter, for financial support. Parts of this research were carried out at PETRA III and University of Hamburg. Ankita Negi, Leon Merten Lohse, Lars Bocklage, Guido Meier, and Ralf Röhlsberger are part of the Cluster of Excellence "CUI: Advanced Imaging of Matter" of the Deutsche Forschungsgemeinschaft (DFG)—EXC 2056—project ID 390715994.

Disclosures. The authors declare no conflicts of interest.

Data availability. Data and analysis scripts underlying the results presented in this paper are available in Ref. [91].

Supplemental document. See Supplement 1 for supporting content.

REFERENCES

- L. Auslander and R. Tolimieri, "Radar ambiguity functions and group theory," SIAM J. Math. Anal. 16, 577–601 (1985).
- A. Bonami, G. Garrigós, and P. Jaming, "Discrete radar ambiguity problems," Appl. Comput. Harmon. Anal. 23, 388–414 (2007).
- C. Fienup and J. Dainty, "Phase retrieval and image reconstruction for astronomy," Image Recovery Theory Appl. 231, 275 (1987).
- J. E. Krist and C. J. Burrows, "Phase-retrieval analysis of pre- and postrepair Hubble Space Telescope images," Appl. Opt. 34, 4951–4964 (1995).
- D. Kermisch, "Image reconstruction from phase information only," J. Opt. Soc. Am. 60, 15 (1970).
- Y. Shechtman, Y. C. Eldar, O. Cohen, et al., "Phase retrieval with application to optical imaging: a contemporary overview," IEEE Signal Process Mag. 32 (3), 87–109 (2015).
- J. Miao, P. Charalambous, J. Kirz, et al., "Extending the methodology of X-ray crystallography to allow imaging of micrometre-sized non-crystalline specimens," Nature 400, 342–344 (1999).
- H. N. Chapman, A. Barty, M. J. Bogan, et al., "Femtosecond diffractive imaging with a soft-X-ray free-electron laser," Nat. Phys. 2, 839–843 (2006).
- R. W. Harrison, "Phase problem in crystallography," J. Opt. Soc. Am. A 10, 1046 (1993).
- W. Coene, G. Janssen, M. Op de Beeck, et al., "Phase retrieval through focus variation for ultra-resolution in field-emission transmission electron microscopy," Phys. Rev. Lett. 69, 3743–3746 (1992).
- 11. B. E. Allman, P. J. McMahon, K. A. Nugent, et al., "Phase radiography with neutrons," Nature 408, 158–159 (2000).
- J. Va'vra, D. Leith, B. Ratcliff, et al., "Beam test of a time-of-flight detector prototype," Nucl. Instrum. Methods Phys. Res. Sect. A 606, 404–410 (2009)
- A. S. Tremsin, J. V. Vallerga, O. H. W. Siegmund, et al., "Photonicscounting MCP/Timepix detectors for soft X-ray imaging and spectroscopic applications," J. Synchrotron. Radiat. 28, 1069–1080 (2021).
- J. R. Fienup, "Phase retrieval algorithms: a comparison," Appl. Opt. 21, 2758 (1982).
- E. J. Candès, X. Li, and M. Soltanolkotabi, "Phase retrieval from coded diffraction patterns," Appl. Comput. Harmon. Anal. 39, 277–299 (2015).
- C. Metzler, P. Schniter, A. Veeraraghavan, et al., "prDeep: robust phase retrieval with a flexible deep network," in Proceedings of the 35th International Conference on Machine Learning, Vol. 80 of Proceedings of Machine Learning Research (PMLR), J. Dy and A. Krause, eds. (2018), pp. 3501–3510.
- 17. K. Cowtan, *Phase Problem in X-ray Crystallography, and its Solution* (Encyclopedia of Life Sciences, 2003).
- R. Beinert and G. Plonka, "Ambiguities in one-dimensional discrete phase retrieval from Fourier magnitudes," J. Fourier Anal. Appl. 21, 1169–1198 (2015).
- M. H. Hayes and J. H. McClellan, "Reducible polynomials in more than one variable," Proc. IEEE 70, 197–198 (1982).
- R. Beinert and G. Plonka, "Enforcing uniqueness in one-dimensional phase retrieval by additional signal information in time domain," Appl. Comput. Harmon. Anal. 45, 505–525 (2018).
- R. Trebino and D. J. Kane, "Using phase retrieval to measure the intensity and phase of ultrashort pulses: frequency-resolved optical gating," J. Opt. Soc. Am. A 10, 1101 (1993).

- D. Spangenberg, E. Rohwer, M. H. Brügmann, et al., "Ptychographic ultrafast pulse reconstruction," Opt. Lett. 40, 1002 (2015).
- R. Trebino, K. W. DeLong, D. N. Fittinghoff, et al., "Measuring ultrashort laser pulses in the time-frequency domain using frequency-resolved optical gating," Rev. Sci. Instrum. 68, 3277–3295 (1997).
- K. Jaganathan, Y. C. Eldar, and B. Hassibi, "STFT phase retrieval: uniqueness guarantees and recovery algorithms," IEEE J. Sel. Top. Signal Process. 10, 770–781 (2016).
- D. Griffin and J. Lim, "Signal estimation from modified short-time Fourier transform," IEEE Trans. Acoust. Speech Signal Process. 32, 236–243 (1984).
- R. L. Mössbauer, "Kernresonanzfluoreszenz von Gammastrahlung in Ir 191," Z. für Physik 151, 124–143 (1958).
- B. Ko, E. Greenberg, V. Prakapenka, et al., "Calcium dissolution in bridgmanite in the Earth's deep mantle," Nature 611, 88–92 (2022).
- S. H. Lohaus, M. Heine, P. Guzman, et al., "A thermodynamic explanation of the Invar effect," Nat. Phys. 19, 1642–1648 (2023).
- M. Miglierini, V. Prochazka, S. Stankov, et al., "Crystallization kinetics of nanocrystalline alloys revealed by in situ nuclear forward scattering of synchrotron radiation," Phys. Rev. B 86, 020202 (2012).
- Y. V. Knyazev, A. I. Chumakov, A. A. Dubrovskiy, et al., "Nuclear forward scattering application to the spiral magnetic structure study in ε-Fe₂O₃," Phys. Rev. B 101, 094408 (2020).
- C. Fadley, "X-ray photoelectron spectroscopy: progress and perspectives," J. Electron. Spectrosc. Relat. Phenom. 178–179, 2–32 (2010).
- R. Egerton, "Limits to the spatial, energy and momentum resolution of electron energy-loss spectroscopy," Ultramicroscopy 107, 575–586 (2007).
- D. Bessas, D. G. Merkel, A. I. Chumakov, et al., "Nuclear forward scattering of synchrotron radiation by ⁹⁹Ru," Phys. Rev. Lett. 113, 147601 (2014).
- A. G. Gavriliuk, V. V. Struzhkin, I. S. Lyubutin, et al., "Another mechanism for the insulator-metal transition observed in Mott insulators," Phys. Rev. B 77, 155112 (2008).
- K. Kothapalli, E. Kim, T. Kolodziej, et al., "Nuclear forward scattering and first-principles studies of the iron oxide phase Fe₄O₅," Phys. Rev. B 90, 024430 (2014).
- G. V. Smirnov, U. van Bürck, A. I. Chumakov, et al., "Synchrotron Mössbauer source," Phys. Rev. B 55, 5811–5815 (1997).
- V. Potapkin, A. I. Chumakov, G. V. Smirnov, et al., "The ⁵⁷Fe synchrotron Mössbauer source at the ESRF," J. Synchrotron. Radiat. 19, 559–569 (2012).
- S. Yaroslavtsev and A. I. Chumakov, "Synchrotron Mössbauer source: trade-off between intensity and linewidth," J. Synchrotron. Radiat. 29, 1329–1337 (2022).
- G. V. Smirnov, "General properties of nuclear resonant scattering," Hyperfine Interact. 123, 31–77 (1999).
- J. P. Hannon and G. T. Trammell, "Coherent-ray optics," Hyperfine Interact. 123, 127–274 (1999).
- G. V. Smirnov, U. van Bürck, W. Potzel, et al., "Propagation of nuclear polaritons through a two-target system: effect of inversion of targets," Phys. Rev. A 71, 023804 (2005).
- 42. R. Röhlsberger, "Nuclear Condensed Matter Physics with Synchrotron Radiation," in *Springer Tracts in Modern Physics* (Springer Berlin Heidelberg, 2005), Vol. **208**.
- 43. W. Sturhahn, "CONUSS and PHOENIX: evaluation of nuclear resonant scattering data," Hyperfine Interact. **125**, 149–172 (2000).
- L. Bocklage, "Nexus-Nuclear Elastic X-ray scattering Universal Software," Zenodo (2024), https://zenodo.org/doi/10.5281/ zenodo.7716207.
- Y. Hasegawa, Y. Yoda, K. Izumi, et al., "Time-delayed interferometry with nuclear resonant scattering of synchrotron radiation," Jpn. J. Appl. Phys. 33, L772 (1994).
- K. Izumi, Y. Yoda, T. Ishikawa, et al., "Time domain interferometry in X-ray region using nuclear resonant scattering," Jpn. J. Appl. Phys. 34, 4258 (1995).
- R. Callens, C. L'abbé, J. Meersschaut, et al., "Phase determination in nuclear resonant scattering using a velocity drive as an interferometer and phase shifter," Phys. Rev. B 72, 081402 (2005).
- L. Wolff and J. Evers, "Unraveling time- and frequency-resolved nuclear resonant scattering spectra," Phys. Rev. Res. 5, 013071 (2023).

- W. Potzel, U. van Bürck, P. Schindelmann, et al., "Investigation of radiative coupling and of enlarged decay rates of nuclear oscillators," Phys. Rev. A 63, 043810 (2001).
- U. van Bürck, W. Potzel, P. Schindelmann, et al., "Inversion of target sequence in nuclear forward scattering of synchrotron radiation," Hyperfine Interact. 141, 151–155 (2002).
- B. Sahoo, K. Schlage, J. Major, et al., "Preparation and characterization of ultrathin stainless steel films," in AIP Conference Proceedings (AIP, 2011), pp. 57–60.
- H. M. L. Faulkner and J. M. Rodenburg, "Movable aperture lensless transmission microscopy: a novel phase retrieval algorithm," Phys. Rev. Lett. 93, 023903 (2004).
- 53. J. Haber, "Hard X-ray quantum optics in thin-film nanostructures," Ph.D. thesis (Universität Hamburg, 2017).
- R. Röhlsberger, H.-C. Wille, K. Schlage, et al., "Electromagnetically induced transparency with resonant nuclei in a cavity," Nature 482, 199–203 (2012).
- 55. R. Röhlsberger, K. Schlage, B. Sahoo, et al., "Collective Lamb shift in single-photonics superradiance," Science **328**, 1248–1251 (2010).
- T. J. Bürvenich, J. Evers, and C. H. Keitel, "Nuclear quantum optics with X-ray laser pulses," Phys. Rev. Lett. 96, 142501 (2006).
- 57. J. Haber, K. S. Schulze, K. Schlage, et al., "Collective strong coupling of X-rays and nuclei in a nuclear optical lattice," Nat. Photonics 10, 445–449 (2016).
- R. Coussement, Y. Rostovtsev, J. Odeurs, et al., "Controlling absorption of gamma radiation via nuclear level anticrossing," Phys. Rev. Lett. 89, 107601 (2002).
- 59. W.-T. Liao and S. Ahrens, "Gravitational and relativistic deflection of X-ray superradiance," Nat. Photonics 9, 169–173 (2015).
- P.-H. Lin, Y.-H. Kuan, Y.-Y. Fu, et al., "Time-delayed magnetic control of X-ray spectral enhancement in two-target nuclear forward scattering," Phys. Rev. Appl. 18, L051001 (2022).
- S. Velten, L. Bocklage, X. Zhang, et al., "Nuclear quantum memory for hard X-ray photonics wave packets," Sci. Adv. 10, eadn9825 (2024).
- I. Tittonen, M. Lippmaa, P. Helistö, et al., "Stepwise phase modulation of recoilless gamma radiation in a coincidence experiment: Gamma echo," Phys. Rev. B 47, 7840–7846 (1993).
- K. P. Heeg, J. Haber, D. Schumacher, et al., "Tunable subluminal propagation of narrow-band X-ray pulses," Phys. Rev. Lett. 114, 203601 (2015).
- L. Bocklage, J. Gollwitzer, C. Strohm, et al., "Coherent control of collective nuclear quantum states via transient magnons," Sci. Adv. 7, eabc3991 (2021).
- P. Thibault, M. Dierolf, O. Bunk, et al., "Probe retrieval in ptychographic coherent diffractive imaging," Ultramicroscopy 109, 338–343 (2009).
- 66. A. Fannjiang and P. Chen, "Blind ptychography: uniqueness and ambiguities," Inverse Prob. **36**, 045005 (2020).
- Z. Yuan, H. Wang, Z. Li, et al., "Nuclear phase retrieval spectroscopy using resonant X-ray scattering," Nat. Commun. 16, 3096 (2025).
- Y. V. Shvyd'ko, U. van Bürck, W. Potzel, et al., "Hybrid beat in nuclear forward scattering of synchrotron radiation," Phys. Rev. B 57, 3552–3561 (1998).
- G. Zheng, R. Horstmeyer, and C. Yang, "Wide-field, high-resolution Fourier ptychographic microscopy," Nat. Photonics 7, 739–745 (2013).
- Y. Jiang, Z. Chen, Y. Han, et al., "Electron ptychography of 2D materials to deep sub-ångström resolution," Nature 559, 343–349 (2018).
- 71. M. Holler, A. Diaz, M. Guizar-Sicairos, et al., "X-ray ptychographic computed tomography at 16 nm isotropic 3D resolution," Sci. Rep. 4, 3857
- A. Walther, "The question of phase retrieval in optics," Opt. Acta Int. J. Opt. 10, 41–49 (1963).
- P. Grohs, S. Koppensteiner, and M. Rathmair, "Phase retrieval: uniqueness and stability," SIAM Rev. 62, 301–350 (2020).
- 74. M. Guizar-Sicairos and P. Thibault, "Ptychography: a solution to the phase problem," Phys. Today **74**, 42–48 (2021).
- A. Schropp and C. G. Schroer, "Dose requirements for resolving a given feature in an object by coherent X-ray diffraction imaging," New J. Phys. 12, 035016 (2010).
- J. Clark, X. Huang, R. Harder, et al., "High-resolution three-dimensional partially coherent diffraction imaging," Nat. Commun. 3, 993 (2012).
- P. Thibault and M. Guizar-Sicairos, "Maximum-likelihood refinement for coherent diffractive imaging," New J. Phys. 14, 063004 (2012).

- S. Chen, J. Montgomery, and A. Bolufé-Röhler, "Measuring the curse of dimensionality and its effects on particle swarm optimization and differential evolution," Appl. Intell. 42, 514–526 (2014).
- D. Guirguis, N. Aulig, R. Picelli, et al., "Evolutionary black-box topology optimization: challenges and promises," IEEE Trans. Evol. Comput. 24, 613–633 (2020).
- B. Polyak, "Some methods of speeding up the convergence of iteration methods," USSR Comput. Math. Math. Phys. 4, 1–17 (1964).
- H. Robbins and S. Monro, "A stochastic approximation method," Ann. Math. Stat. 22, 400–407 (1951).
- A. Negi and L. M. Lohse, "NuPty-Nuclear Ptychography with PyTorch," Zenodo (2025), https://zenodo.org/doi/10.5281/zenodo.15516914.
- 83. A. Paszke, S. Gross, F. Massa, et al., "PyTorch: an imperative style, highperformance deep learning library," arXiv (2019).
- P. Thibault and A. Menzel, "Reconstructing state mixtures from diffraction measurements," Nature 494, 68–71 (2013).
- P. Li, T. Edo, D. Batey, et al., "Breaking ambiguities in mixed state ptychography," Opt. Express 24, 9038–9052 (2016).

- A. Dejkameh, R. Nebling, U. Locans, et al., "Recovery of spatial frequencies in coherent diffraction imaging in the presence of a central obscuration," Ultramicroscopy 258, 113912 (2024).
- 87. J. Reinhardt, R. Hoppe, G. Hofmann, et al., "Beamstop-based low-background ptychography to image weakly scattering objects," Ultramicroscopy **173**, 52–57 (2017).
- K. P. Heeg, H.-C. Wille, K. Schlage, et al., "Vacuum-assisted generation and control of atomic coherences at X-ray energies," Phys. Rev. Lett. 111, 073601 (2013).
- 89. D. Bessas, I. Sergueev, K. Glazyrin, et al., "Revealing the hidden hyperfine interactions in ϵ -iron," Phys. Rev. B **101**, 035112 (2020).
- 90. R. D. Taylor, G. Cort, and J. O. Willis, "Internal magnetic fields in hcp-iron," J. Appl. Phys. **53**, 8199–8201 (1982).
- A. Negi, "Dataset for energy-time ptychography for onedimensional phase retrieval," Zenodo (2025), https://zenodo.org/doi/ 10.5281/zenodo.15521341.